JACS
JOURNAL OF THE AMERICAN CHEMICAL SOCIETY
Article
pubs.acs.org/JACS

High Electrocatalytic Hydrogen Evolution Activity of an Anomalous Ruthenium Catalyst

Yao Zheng,[†,⊥] Yan Jiao,[†,⊥] Yihan Zhu,[‡,⊥] Lu Hua Li,[§] Yu Han,[‡] Ying Chen,[§] Mietek Jaroniec,[∥] and Shi-Zhang Qiao*[,†]

[†]School of Chemical Engineering, University of Adelaide, Adelaide, South Australia 5005, Australia
[‡]Advanced Membranes and Porous Materials Center, Physical Sciences and Engineering Division, Imaging and Characterization Core Lab, King Abdullah University of Science and Technology, Thuwal 23955-6900, Saudi Arabia
[§]Institute for Frontier Materials, Deakin University, Waurn Ponds, Victoria 3216, Australia
[∥]Department of Chemistry and Biochemistry, Kent State University, Kent, Ohio 44242, United States

Supporting Information

ABSTRACT: Hydrogen evolution reaction (HER) is a critical process due to its fundamental role in electrocatalysis. Practically, the development of high-performance electrocatalysts for HER in alkaline media is of great importance for the conversion of renewable energy to hydrogen fuel via photoelectrochemical water splitting. However, both mechanistic exploration and materials development for HER under alkaline conditions are very limited. Precious Pt metal, which still serves as the state-of-the-art catalyst for HER, is unable to guarantee a sustainable hydrogen supply. Here we report an anomalously structured Ru catalyst that shows 2.5 times higher hydrogen generation rate than Pt and is among the most active HER electrocatalysts yet reported in alkaline solutions. The identification of new face-centered cubic crystallographic structure of Ru nanoparticles was investigated by high-resolution transmission electron microscopy imaging, and its formation mechanism was revealed by spectroscopic characterization and theoretical analysis. For the first time, it is found that the Ru nanocatalyst showed a pronounced effect of the crystal structure on the electrocatalytic activity tested under different conditions. The combination of electrochemical reaction rate measurements and density functional theory computation shows that the high activity of anomalous Ru catalyst in alkaline solution originates from its suitable adsorption energies to some key reaction intermediates and reaction kinetics in the HER process.

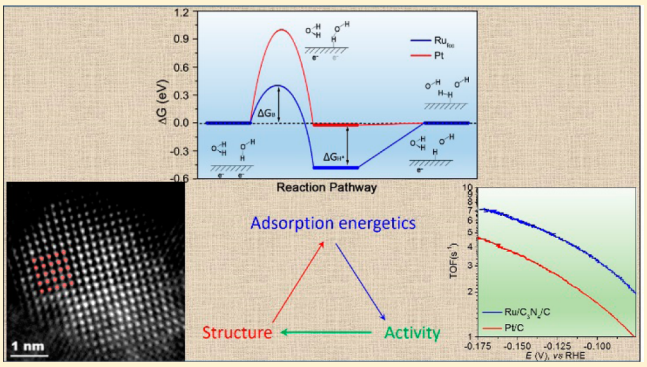

INTRODUCTION

The search for suitable catalysts with maximum mass-specific reactivity yet long-term stability has been an everlasting but still formidable challenging topic in catalysis research. Generally, the apparent rate of a surface reaction occurring on a heterogeneous catalyst is strongly dependent on its geometric properties (size, conformation, crystallinity, etc.) and electronic structure (d-band center position, work functions, etc.), which act together in determining adsorption of intermediates, activation energies, and energy barriers for this reaction.[1−7] This complexity hinders the design and selection of the most appropriate catalyst for a specific catalytic reaction. For instance, one catalyst's geometric structure sensitivity can significantly affect its activity toward a specific heterogeneous reaction like the ammonia synthesis over certain iron crystal faces,[5] crystallographic dependence of Fischer−Tropsch process over cobalt catalysts,[6] and nanogold's size dependence of carbon monoxide oxidation.[7]

Due to the enormous advances in modern physical chemistry and computational quantum chemistry, an in-depth understanding of the macroscopic reaction kinetics of catalytic processes at the atomic level can be achieved by correlating reaction rate measurements, spectroscopic characterization, and theoretical calculations.[3,8−10] The importance of this correlation lies in its ability to reveal the nature of the solid catalysts and the origin of their reactivity toward specific catalytic processes.[11−14] Therefore, one can engineer potential catalysts with desired performance by tailoring their chemical composition and/or physical structure.

Hydrogen evolution ($2H^+ + 2e^- \rightarrow H_2$, HER) is an ideal model reaction for introducing the aforementioned advanced methodology to the field of electrocatalysis. HER generates solely the desired product and is being considered as a cornerstone reaction in exploring the mechanism of more complex multielectron transfer processes.[15,16] Practically, HER is also an essential reaction in the photoelectrochemical (PEC) water splitting for hydrogen production.[17,18] In contrast to the

Received: October 30, 2016
Published: November 28, 2016

DOI: 10.1021/jacs.6b11291
J. Am. Chem. Soc. 2016, 138, 16174−16181

traditional steam reforming of natural gas, the generation of clean hydrogen fuel from water is a potential route toward a sustainable energy future. Although commercial technologies of alkaline electrolysis offer mild conditions and higher system efficiency than acidic proton exchange membrane electrolysis, the reaction rate of HER in alkaline solutions is ∼ 2−3 orders of magnitude lower than that in acidic solutions.[19] More importantly, in the promising PEC water splitting technology, the best oxygen evolution reaction (OER) electrocatalysts used as counter electrodes work well only in basic or neutral media.[18,20,21] Therefore, the development of HER catalysts suitable for alkaline solutions is crucial. Currently, the fundamental studies of HER are mainly conducted under acidic conditions due to its relative simple reaction pathway. The activity origin and trend for a wide variety of metallic electrocatalysts have been successfully constructed.[14,16,22,23] However, the overall comprehension of the HER process in alkaline solutions is very limited, mainly on monocrystalline and polycrystalline Pt surfaces.[19,24,25] As a result, the molecular design and practical development of efficient electrocatalysts for this key but sluggish process have been largely hindered. Evidently, Pt shows an "incomparable" HER activity in alkaline solutions, while all well-developed cost-effective alternatives, including high-surface area Raney Ni and nickel molybdenum alloy, still cannot match the activity of Pt.[26,27] However, its scarcity and high cost cannot afford a sustainable hydrogen generation.

Herein we present the identification of an anomalously structured Ru catalyst, with 1/25 price of Pt metal, that shows 2.5 times higher hydrogen evolution turnover frequency (TOF) under alkaline conditions than the state-of-the-art Pt/C catalyst. Density functional theory (DFT) computation and electrochemical reaction rate measurements were conducted to evaluate the newly developed Ru catalyst by linking its extrinsic crystalline structure with intrinsic reaction energetics in the hydrogen evolution process. Based on the elucidation of poorly known nature of HER in alkaline media, here we reveal for the first time the origin of highest HER activity of this cost-effective catalyst in comparison to all previously reported precious metals, nonprecious metals, and nonmetallic materials.

EXPERIMENTAL AND COMPUTIONAL METHODS

Materials Synthesis. First, a specified amount of diluted $RuCl_3$ aqueous solution (0.005 M) was mixed with dicyandiamide (DCDA) to make a homogeneous solution; namely, 80 mL of $RuCl_3$ aqueous solution and 1 g of DCDA solid were used to achieve the resultant Ru-graphitic carbon nitride complex supported on carbon ($Ru/C_3N_4/C$) containing ∼20 wt % of metallic Ru (confirmed by thermogravimetric analysis as shown in Figure S1), which is comparable with 20 wt % of metallic Pt in commercial Pt/C benchmark. Then the mixture was concentrated using a rotary evaporator and dried using a freeze-dryer. The collected dark powder was then annealed under argon atmosphere at 600 °C for 1 h at a heating rate of 2 °C min^{-1}. In the presence of Ru catalyst, most of the DCDA precursor did not follow the rational reaction path of polycondensation to obtain the periodic g-C_3N_4 matrix but was converted to nitrogen-doped carbon, as confirmed by the carbon K-edge near edge X-ray absorption fine structure (NEXAFS) results. Pure Ru supported on carbon (Ru/C) was prepared by mixing 0.005 M $RuCl_3$ aqueous solution with oxidized commercial carbon black. Then, the mixture was dried and annealed using the same procedure as in the synthesis of $Ru/C_3N_4/C$ and used as a control sample. Commercial platinum carbon (Pt/C with 20 wt % Pt), iridium carbon (Ir/C with 20 wt % Ir), palladium carbon (Pd/C with 20 wt % Pd), and gold carbon (Au/C with 20 wt % Au) catalysts were purchased from the Fuel Cell Store without any further treatment.

Material Characterization. Scanning transmission electron microscopy (STEM) and transmission electron microscopy (TEM) images and electron diffraction patterns were collected on a cubed Titan G2 80-300 field emission gun electron microscope equipped with a Fischione model 3000 high-angle annular dark-field (HAADF) detector and a CEOS GmbH double-hexapole spherical-aberration corrector operating at 300 kV. A probe semiconvergence angle of 24.9 mrad was used for STEM imaging. Some raw HAADF-STEM images were processed by masking diffraction spots in the fast-Fourier transforms of the original images and then back-transforming using a Gatan Digital Micrograph.

The NEXAFS measurements were carried out in an ultrahigh vacuum chamber ($\sim 10^{-10}$ mbar) of the undulator soft X-ray spectroscopy beamline at the Australian Synchrotron. The samples were dispersed in deionized water and then deposited and dried on Au plates. The raw NEXAFS data were normalized to the photoelectron current of the photon beam, measured on an Au grid. The C K-edge spectra were double corrected to remove the influence from adsorbed carbon on the optics and detector.

Electrochemical Testing Setup. The as-prepared powder was first ultrasonically dispersed in distilled water (Milli-Q) containing 0.05 wt % of Nafion. Twenty μL of aqueous dispersion of the catalyst (2.0 mg/mL) was then transferred onto the glassy carbon rotating disk electrode (RDE, 0.196 cm^2, Pine Research Instrumentation) serving as a working electrode. The reference electrode was an Ag/AgCl in 4 M KCl solution, and the counter electrode was a graphite rod. All potentials were referenced to reversible hydrogen electrode (RHE) by using pure hydrogen calibration, and all polarization curves were corrected for the *iR* contribution within the cell. During experiments a flow of N_2 was maintained over the electrolytes used: 0.5 M H_2SO_4, or 0.1 M KOH solution. The working electrode was rotated at 1600 rpm to remove hydrogen gas bubbles formed at the catalyst surface.

Computational Methods and Models. The electronic structure computation was conducted by using VASP code.[28−31] To describe the electron−core interaction, the projector-augmented wave (PAW) method was utilized within the frozen-core approximations for Ru and Pt.[32,33] For electron exchange−correlation, the Perdew−Burke−Ernzerhof (PBE) functional within the generalized-gradient approximation (GGA) range was applied.[34,35] The cutoff energies for plane waves were chosen to be 400 eV based on the convergence test on Ru_{hcp} 3 × 3 supercell and 5 × 5 Ru + g-C_3N_4 supercell. The convergence tolerance of force on each atom during structure relaxation was set to be 0.01 eV/Å, and all atoms were allowed to relax. Spin-polarization effect was considered in all cases. To better describe the dispersion interaction within water adsorption systems, vdW correction was considered by adopting the Grimme's D2 scheme.[36] The parameters for Ru, O, and H are the default values given by VASP 5.3, and those for Pt are C_6 = 4.43 J·nm^6·mol^{-1} and R_0 = 1.772 Å.[37] The cutoff radius (Å) for pair interactions among D2 scheme is set to be 20 Å to avoid interactions between different layers, with global scaling factor set to be 0.750 Å. The optimized lattice parameters for hexagonal close-packed (hcp) Ru ($a = b$ = 2.73 Å, c = 4.31 Å), face-centered cubic (fcc) Ru (3.82 Å), and fcc Pt (3.97 Å) structures agree well with previous computation studies.[38−41] The K-point for all three metal (1 × 1) single cell, ($\sqrt{3} \times \sqrt{3}$) reconstructed surface, (1 × 1) g-C_3N_4, and (5 × 5) metal with (2 × 2) g-C_3N_4 was set to be 15 × 15 × 15, 9 × 9 × 1, 5 × 5 × 1, and 1 × 1 × 1, respectively.

The calculation of adhesion energy between Ru and g-C_3N_4 was modeled for three layers of Ru slab, one layer of g-C_3N_4, and a 16 Å vacuum layer to separate the interaction between periodic images. This supercell structure contains a (5 × 5) lattice of $Ru_{hcp}(0001)$ or $Ru_{fcc}(111)$ primitive cells matched to (2 × 2) lattice of repeating g-C_3N_4 primitive cells. Three configurations with different relative position between metals and g-C_3N_4 were investigated, i.e., FCC, HCP, and TOP positions, according to the position of C_6N_7 rings in g-C_3N_4 matrix on the top layer of Ru atoms. The calculation of adhesion energy between Ru and carbon was modeled by three layers of (1 × 1)

DOI: 10.1021/jacs.6b11291
J. Am. Chem. Soc. 2016, 138, 16174−16181

$Ru_{hcp}(0001)$ or $Ru_{fcc}(111)$ and one layer of (1 × 1) graphene to represent carbon black. Similarly, three relative configurations were studied due to the lattice mismatch between Ru and graphene, as in the previous work.[42] More computational details about free energy diagram, water dissociation pathway, and H_2 recombination pathway can be found in the Supporting Information.

RESULTS AND DISCUSSION

Structural Identification. The as-synthesized $Ru/C_3N_4/C$ product shows a homogeneous dispersion of Ru nanoparticles with an average size of 2 nm on the g-C_3N_4/C support (Figure S2). Note that we did not carry out the conventional synthesis of precious metal nanoparticles involving bulky capping, structure-directing, or reducing agents, etc. The formation of homogeneous particle size of Ru was achieved by taking advantage of strong interaction (discussed later) between Ru metal and g-C_3N_4 support that has a periodically regular molecular structure. The HAADF-STEM images provide more structural information about these Ru nanoparticles (Figure 1a,c,e). Normally, the majority of metals show only its most stable crystalline structure: either a fcc, a body centered cubic (bcc), or a hcp structure. The structure transition can only be achieved under some extreme conditions, e.g., temperature and/or pressure and may lead to some unique electrical, magnetic, and catalytic properties as compared with the most stable structures under ambient conditions.[43−45] Ru as a 4d transition-metal possesses an hcp structure, as reported in most experimental and theoretical studies.[46−48]

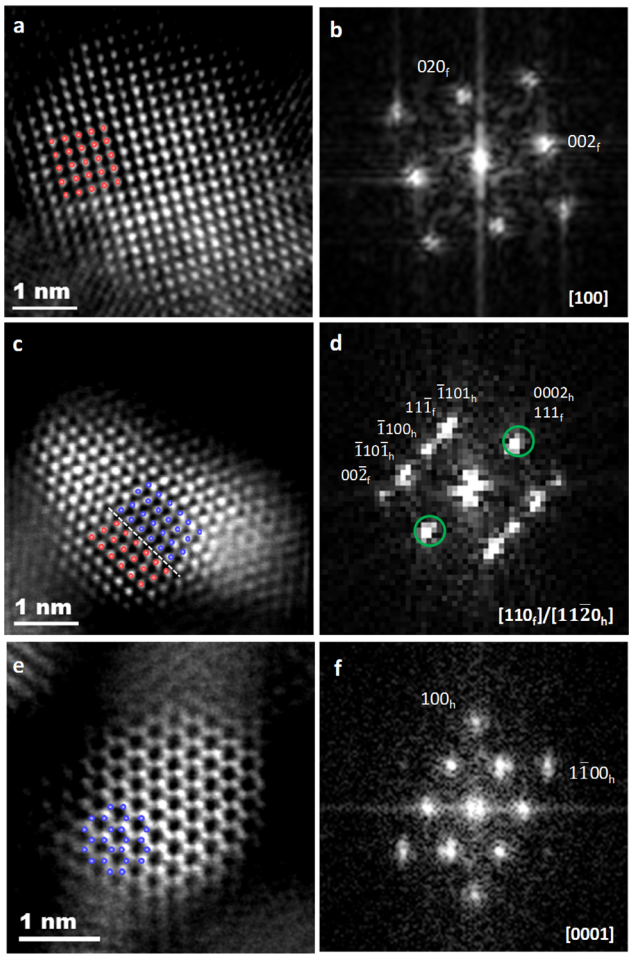

Figure 1. (a,c,e) HAADF-STEM images and the (b,d,f) corresponding FFT patterns of Ru nanoparticles showing (a) fcc; (c) mixed fcc/hcp; and (e) hcp structure. The red and blue dots in panels a, c, e mark the typical atomic arrangements of fcc and hcp structures along different zone axes. The green circles in panel d inset indicate the shared diffraction plans of the fcc and hcp structures.

Interestingly, the typical atomic resolution HAADF-STEM images of individual Ru nanoparticles in $Ru/C_3N_4/C$ catalyst were used to unambiguously identify a typical $[100]_f$ oriented fcc monophase, a $[110]_f/[11\bar{2}0]_h$ oriented intergrown hcp/fcc phase sharing the $(0001)_h/(111)_f$ interface, and a $[0001]_h$ oriented hcp monophase, respectively. These results are further supported by the indexed fast Fourier transform (FFT) diffractograms (Figure 1b,d,f) and high-resolution TEM images (Figure S3). In addition, in comparison with a Ru/C control sample that only demonstrates hcp Ru crystal on the electron diffraction patterns (Figure S4), $Ru/C_3N_4/C$ shows an extra intensity at ~7.3 nm^{-1} that can be assigned to the (022) reflection of the fcc Ru crystal. Given the difference between two materials is the existence of g-C_3N_4,[49] we assume that g-C_3N_4 as the support allows for the growth of the anomalous fcc Ru lattice structure. Similarly to the Kitagawa et al. report on the formation of multiply twinned Ru particles based on the "nanosize" effect,[46] our study shows clearly that the anomalous Ru structures exist in the case of small nanosized particles confined by the g-C_3N_4 phase.

Adhesion Energy Calculation. To validate the above assumption, the DFT calculated adhesion energies (ΔE_{adh}) between two specific Ru nanostructures and g-C_3N_4 substrate were used to quantitatively describe the formation mechanism of anomalous Ru crystalline structure (Figures 2a and S5 and Table S1). For comparison purposes, the values of ΔE_{adh} between Ru and pure carbon layer represented by graphene were also computed (Figure S6 and Table S1). For standalone Ru slabs, the hcp structure is more stable than the fcc one with an energy difference of 0.06 eV per Ru atom, which is in good agreement with previous experimental observations.[46−48] Conversely, as shown in Figure 2b (dashed bars), the ΔE_{adh} calculated for fcc structured Ru (Ru_{fcc}) on the g-C_3N_4 substrate is nearly 4 eV (0.15 eV per Ru atom on the top layer) higher

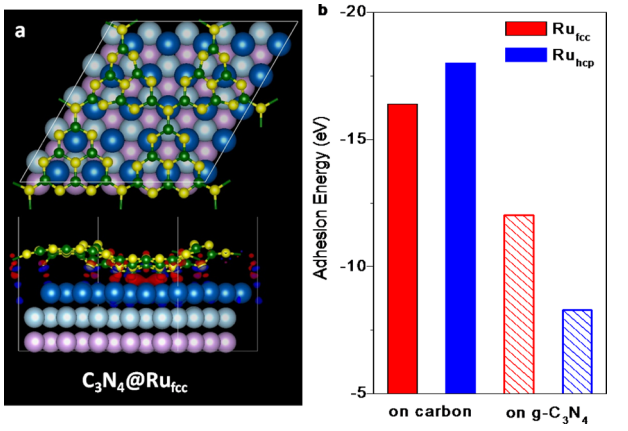

Figure 2. (a) Atomic configurations (tops) and side views of the electron difference (bottoms) of g-C_3N_4 (2 × 2) and Ru (5 × 5) layers with fcc structure. Color codes: Deep blue, light blue and pink denote the top, middle, and bottom layer of Ru atoms, respectively; green and yellow denote carbon and nitrogen atoms in g-C_3N_4 layer, respectively. (b) Comparison of the adhesion energy between carbon/g-C_3N_4 and Ru layers with fcc or hcp structure.

DOI: 10.1021/jacs.6b11291
J. Am. Chem. Soc. 2016, 138, 16174−16181

than that of hcp structured Ru (Ru_{hcp}), confirming the stabilizing effect of g-C_3N_4 toward formation of Ru_{fcc} achieved by enhanced metal−substrate interactions. On the other hand, such tendency was not observed in the case of a carbon substrate, on which the Ru_{hcp} structure is more energetically favorable than Ru_{fcc} as indicated by a larger ΔE_{adh} (Figure 2b solid bars). Thus, g-C_3N_4 acts as a promoter that can facilitate the formation of anomalous fcc crystalline Ru structure. This theoretically predicted result agrees with the experimental data showing that there is a certain amount of fcc crystalline Ru in the Ru/C_3N_4/C composite, while only a sole hcp phase exists in the Ru/C control sample (Figure S4). Besides crystalline, the rich functional groups in g-C_3N_4 molecular skeleton (e.g., triazine, amine, etc.) may also modulate the growth of Ru nanoparticles, resulting in a more uniform distribution and smaller size than those grown on clean carbon surfaces (Figure S2).

Chemical Characteristics of Ru/C_3N_4/C. NEXAFS spectroscopy was used to precisely detect intramolecular interactions between Ru and g-C_3N_4, as demonstrated by the DFT calculations. In the C K-edge region (Figure 3a), the Ru/C_3N_4/C catalyst mainly shows the characteristic resonances of π^*_{C-N-C}, $\pi^*_{C=C}$, and π^*_{C-N} originating from g-C_3N_4 and nitrogen-doped carbon (N-carbon) supports (the identification of each characteristic resonance can be referred to Figure 3 caption). This not only confirms the existence of N-carbon in Ru/C_3N_4/C composite but also indicates that Ru has no noticeable effect on the chemical environment of carbon. In the N K-edge region (Figure 3b), besides expected pyridinic and graphitic nitrogen species' resonances from N-carbon individual component, the C−N−C coordination in Ru/C_3N_4/C was preserved, while the original bridging N resonance in g-C_3N_4 was weakened and accompanied by a group of new peaks in the lower photon energy zone (the identification of each characteristic resonance can be referred to Figure 3b caption). These new nitrogen resonances can be assigned to the interaction of Ru with bridging N−3C species of g-C_3N_4 with different coordination. As a result, nitrogen atoms accept extra charges from Ru atom, resulting in a negative shift in its photon energy profile.

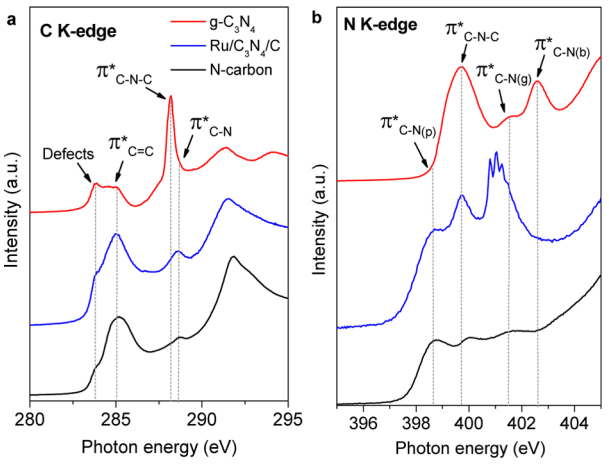

Figure 3. C K-edge and N K-edge NEXAFS spectra of Ru/C_3N_4/C electrocatalyst, pure g-C_3N_4, and N-carbon reference samples. In C K-edge, defects at ~283 eV in all three materials are assigned to low-coordinated carbon atoms at the edges of g-C_3N_4 and N-carbon moieties. The resonances of π^* at 288.2 eV are assigned to C−N−C species in g-C_3N_4, while the resonances of π^* at 285.0 eV and π^* at 288.7 eV are assigned to C═C and C−N species in N-carbon. In N K-edge, the resonances of π^* at 398.6 and 401.5 eV are assigned to nitrogen species in the form of pyridine (C−N(p)) and graphite (C−N(g)) structures in N-carbon. The resonances of π^* at 399.7 and 402.6 eV are assigned to the aromatic C−N−C coordination of tri-*s*-triazine and the N−3C bridging among three tri-*s*-triazine moieties (C−N(b)) in g-C_3N_4.

Electrocatalytic Activity Comparison. The electrocatalytic properties of the newly identified Ru/C_3N_4/C electrocatalyst were evaluated and compared to the conventional Ru/C and the state-of-the-art Pt/C electrocatalysts under alkaline conditions. The polarization curves of three electrocatalysts recorded in 0.1 M KOH solution show an increase in the HER activity (on the overpotential basis) in the following order: Ru/C < Pt/C < Ru/C_3N_4/C (Figure 4a). The normalized (with

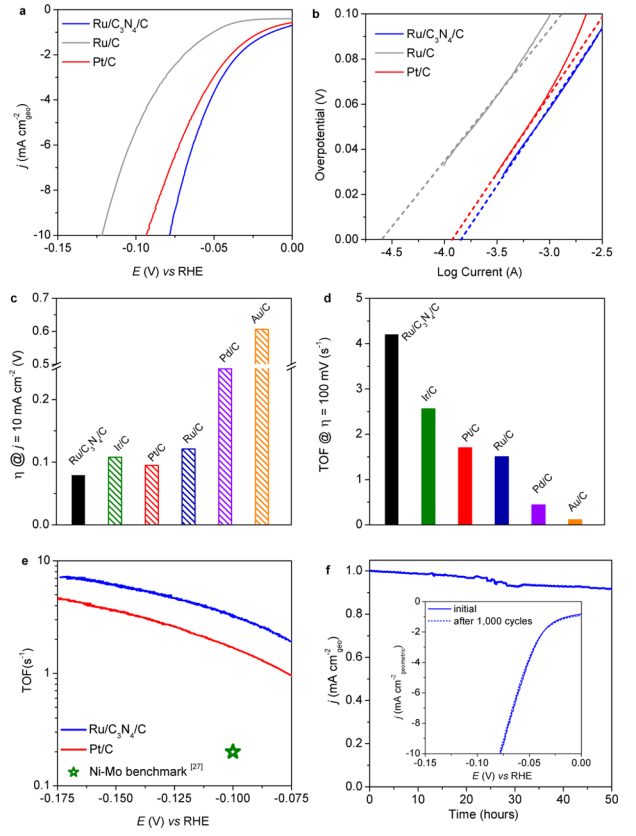

Figure 4. (a) HER polarization curves and (b) corresponding Tafel plots of the Ru/C_3N_4/C, conventional Ru/C, and commercial Pt/C electrocatalysts recorded in N_2-purged 0.1 M KOH solutions. The dashed lines in panels are a guide for the eye to calculate j_0 by the linear fitting of Tafel plots. In panel a, the underpotential hydrogen adsorption effect in the case of precious metals and the capacitance effect in the case of nanocarbons make that the current start points are not zero. (c) Comparison of the overpotential values required to achieve a 10 mA cm^{-2} cathodic current densities and (d) TOF values at 100 mV overpotential in alkaline solutions for various nanostructured precious metal electrocatalysts on carbon support. (e) The relationship between TOF and the measured potentials for the Ru/C_3N_4/C and commercial Pt/C electrocatalysts in 0.1 M KOH solutions. The benchmark according to the metallurgically prepared commercial Ni−Mo alloys.[27] (f) Current−time (*i*−*t*) chronoamperometric response of Ru/C_3N_4/C electrocatalyst at an overpotential of 50 mV. Inset represents HER polarization curves recorded before and after 1000 potential sweeps (+0.2 to −0.6 V versus RHE) in 0.1 M KOH solution.

DOI: 10.1021/jacs.6b11291
J. Am. Chem. Soc. 2016, 138, 16174−16181

respect to the electrode's geometrical area) exchange current density (j_0) values obtained from Tafel plots also follow the same trend (Figure 4b). As read from Figure 4a, a small overpotential of 79 mV was required for achieving a 10 mA cm^{-2} cathodic current density (such current density was chosen as a metrics for the comparison with solar hydrogen production) by the $Ru/C_3N_4/C$ sample. This value is not only much smaller than that for some nonprecious metal HER electrocatalysts like WC,[50] Ni_2P,[51] Mo_2C[52] but also, more strikingly, superior as compared to the values obtained for all reported pure and nanostructured precious metals like Pt,[53] Au,[53,54] Ir,[53] Pd,[54] and Ru itself[53] under the same conditions (Figures 4c and S7a). We note that the performances of individual metal-free components g-C_3N_4, N-carbon, and their hybrid are ignorable as compared with a Ru-containing catalyst, $Ru/C_3N_4/C$ (Figure S8); therefore, a significant enhancement in its activity in comparison to that of the Ru/C control sample can be solely attributed to the presence of anomalous fcc crystalline Ru nanoparticles.

TOF Analysis. To eliminate the contributions originating from different particle sizes and surface areas of electrocatalysts to the measured HER activity, we calibrated the electrochemically active surface area (ECSA) of the newly developed $Ru/C_3N_4/C$ and a series of precious metal electrocatalysts by a well-established cyclic voltammetry method (Figure S9), which has been successfully validated on Ru electrodes surfaces.[55,56] Afterward, the TOF, the best figure-of-merit used for comparative evaluation of the catalytic activities of different catalysts, can be explicitly calculated based on the current density obtained from the polarization curve. As expected,the TOF value increases with the overpotential following the Tafel behavior for all samples. As shown in Figure 4d, at an overpotential of 100 mV, the $Ru/C_3N_4/C$ electrocatalyst exhibits an extremely high TOF of 4.2 s^{-1}, which is larger than that of most commercial precious metal/carbon nanocomposites. Note that the price of Ru metal is at least 10 times cheaper than other precious metals, which is advantageous for the large-scale commercialization in the future (Table S2). Moreover, the TOF value obtained for $Ru/C_3N_4/C$ was also compared with other benchmarked electrocatalysts: it is 60 times larger than that on Ni_5P_4 catalyst (0.06 s^{-1}),[57] 80 times larger than that on Ni−Mo catalyst (0.05 s^{-1}),[27] and most importantly, 2.5 times larger than that on currently the most active Pt/C catalyst under the same conditions (Figure 4e). Additionally, the strong interactions of Ru nanoparticles with g-C_3N_4/C support, as confirmed by both experimental and theoretical studies, prevent its aggregation during long-term reaction. This assures high HER operational stability of the $Ru/C_3N_4/C$ electrocatalyst in alkaline solutions with a very slow attenuation after 50 h (Figure 4f). The accelerated durability test (ADT) also revealed its reliable stability with a very small negative shift of the HER polarization after 1000 continuous potential cycles (Figure 4f inset).

Crystal Structure Sensitivity in Electrocatalysis under Different Conditions. As shown in Figure 5a, $Ru/C_3N_4/C$ also is applicable under acidic conditions, in which the activity is higher than in alkaline solutions. This trend also agrees with other reports on Pt/C materials.[21,24] The activity differences in acid and alkaline solutions can be attributed to the nature of the reaction pathway in each type of solution, which will be discussed in detail later. Additionally, the TOF values of $Ru/C_3N_4/C$ are always higher than that of the Ru/C control sample under the same conditions (Figure 5a,b). This trend is

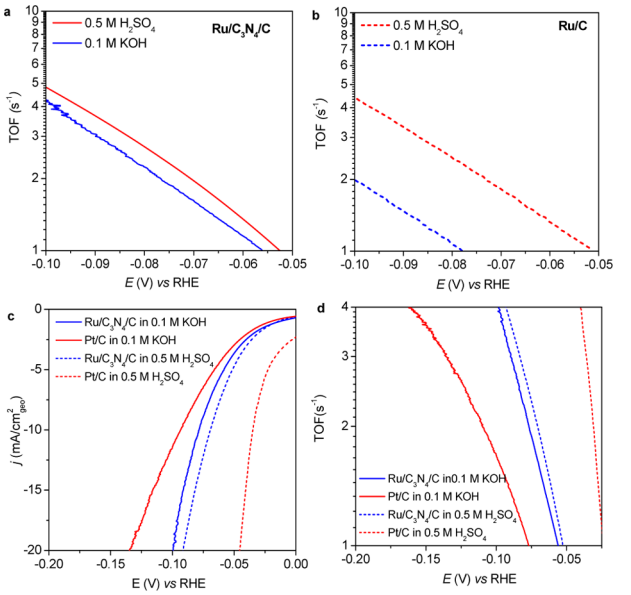

Figure 5. (a,b) The relationship between TOF values and the measured potentials for $Ru/C_3N_4/C$ and conventional Ru/C electrocatalysts under various conditions. (c) Polarization curves and (d) the relationship between TOF values and the measured potentials for the $Ru/C_3N_4/C$ and Pt/C electrocatalysts under various conditions.

more obvious at high pH values than at low pH values. For example, the TOF difference between $Ru/C_3N_4/C$ and Ru/C in acidic solutions is 0.38 s^{-1} at an overpotential of 100 mV (0.05 s^{-1} at an overpotential of 50 mV), while this value is as large as 2.25 s^{-1} at an overpotential of 100 mV (0.45 s^{-1} at an overpotential of 50 mV) in alkaline solutions. Given that the most noticeable difference between these two kinds of catalysts is the crystalline structure of Ru (after ECSA normalization), we attribute the observed difference in the catalytic activities to the Ru crystal structure sensitivity under different testing conditions.

The lattice structure-induced enhancement in the catalytic activity under specific conditions is also reflected between Pt/C and $Ru/C_3N_4/C$ samples. Judged from both overpotential and TOF bases, $Ru/C_3N_4/C$ shows smaller HER activity than that of Pt/C under acid conditions while reversely shows better activity under alkaline conditions (Figure 5c,d). As can be also seen, the activity differences for $Ru/C_3N_4/C$ electrocatalyst in acid and alkaline solutions are small, which is rarely observed on other electrocatalysts because the reaction rate of HER in alkaline solutions is usually ∼2−3 orders of magnitude lower than that in acidic solutions (for example, on Pt surface).[21] Therefore, we assume the reversible activity trend in acid and alkaline solutions should be attributed to some critical but unknown factor(s) that govern the overall reaction rate on each electrocatalyst surface.

Origin of the Enhanced Activity of $Ru/C_3N_4/C$. We performed DFT computations related to the thermodynamics and kinetics of HER on different metal surfaces to reveal the observed activity difference and the origin of the superior activity of $Ru/C_3N_4/C$ in alkaline solutions (Figure 6). Ru slabs with both Ru_{hcp} (0001) and Ru_{fcc} (111) planes were modeled to represent conventional Ru in Ru/C and the newly identified anomalous Ru in $Ru/C_3N_4/C$ sample, respectively; a Pt slab with (111) plane that represents the Pt/C sample was also studied for the purpose of comparison.[13,47] Even though the

DOI: 10.1021/jacs.6b11291
J. Am. Chem. Soc. 2016, 138, 16174−16181

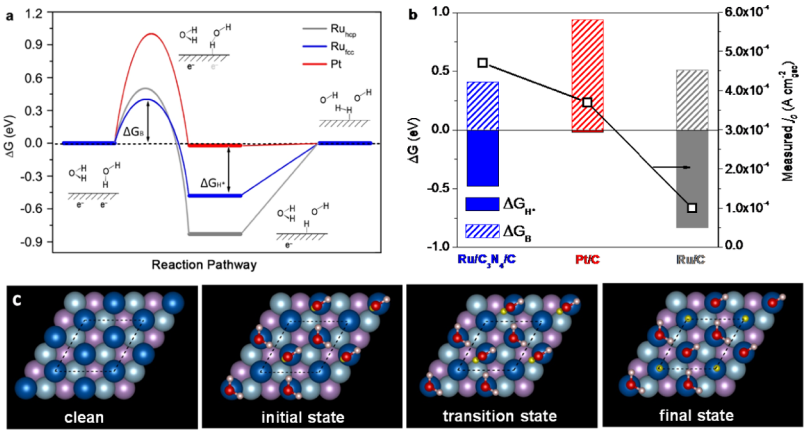

Figure 6. (a) Gibbs free energy diagram of HER on different surfaces including reactant initial state, intermediate state, final state, and an additional transition state representing water dissociation. ΔG_{H^*} indicates hydrogen adsorption free energy, and ΔG_B indicates water dissociation free energy barrier. (b) The relationship between the computed ΔG_{H^*} or ΔG_B values and the measured j_0 values on various metal surfaces. (c) Atomic configurations of water dissociation step on the surface of Ru_{fcc}. Color codes: deep blue, light blue, and pink represent top, middle, and bottom layers of Ru. Red and white represent oxygen and hydrogen atoms in a single water molecule. Yellow represents the dissociated H atom that adsorbs on the metal surface.

computed structured surfaces cannot fully represent the experimentally synthesized metal nanoparticles with various facets, corners, and edges, these specific planes were selected because they are among the most commonly observed and most respective ones in both experiments and theoretical modeling studies.[14,47,58] On all selected metal surfaces, we constructed the reaction pathway for HER including bilayer adsorption of H_2O, dissociation of water to form adsorbed H (H*), combination of H* with proton from adjacent H_2O to form adsorbed H_2, and desorption of H_2 from the surface.[21] As shown in Figure 6a, among all three metal surfaces, Pt shows the optimal level for H adsorption step with a free energy ($\Delta G_{H^*}^{Pt}$) value of −0.02 eV, while Ru_{hcp} and Ru_{fcc} surface exhibit more negative values with $\Delta G_{H^*}^{Ru\text{-}hcp}$ = −0.83 eV and $\Delta G_{H^*}^{Ru\text{-}fcc}$ = −0.48 eV, respectively. Therefore, from the thermodynamic point of view, Pt should demonstrate the best hydrogen evolution activity among these three metal structures. The calculated ΔG_{H^*} values on the respective metal surfaces can be correlated with their electronic structures via the d-band center theory to reveal the origin of their reactivity (Figure S10).[59] The general trend is that with a low position d-band, such as in the case of Pt, the hydrogen adsorption is weak; while for a metal with a higher d-band position, such as Ru_{hcp}, the hydrogen binding is strong thus resulting in a more negative ΔG_{H^*} and is not thermodynamically favorable for the H* desorption process in the Heyrovsky step.

However, the above theoretical investigation based only on adsorption energetics can hardly meet with the experimental observation: comparing with Pt/C, a larger j_0 value was observed on the $Ru/C_3N_4/C$ sample, which is represented by the Ru_{fcc} slab with a relatively stronger H* adsorption (Figure 6b).When the kinetics of water dissociation from the Volmer step is considered, as shown in Figure 6a (curved lines), the Pt surface exhibits a significant energy barrier (ΔG_B = 0.94 eV), substantively higher than that on Ru_{fcc} (ΔG_B = 0.41 eV) and Ru_{hcp} (ΔG_B = 0.51 eV) (Table 3, Figure S11, 12). Therefore, from the kinetic viewpoint, conversely, Pt demonstrates the most sluggish water dissociation among the three metal structures studied. Note that this water dissociation issue does not exist under acidic conditions;[14] therefore Pt shows an extremely high activity in acid solutions, owing to its optimal ΔG_{H^*} value. We conducted further computation work to obtain energy barrier values for the following H_2 formation process by Heyrovsky mechanism on Ru surfaces. As shown in Figure S13, the energy barrier for Heyrovsky step on Ru_{fcc} is 0.48 eV while that on Ru_{hcp} is 0.40 eV (Figure S13). These easily surmountable barrier values indicate that the Heyrovsky step is kinetically viable and does not serve as the limiting step for the overall reaction.

Regarding the overall HER rate, it is generally accepted that ΔG_{H^*} could be employed to obtain the HER rate in acidic solutions based on the microkinetic model.[14] This has also been validated by our computation done for selected models and by measurements performed on the synthesized electrocatalysts (Figure S14). However, with the identification of large energy barrier-like water dissociation on the Pt surface, the ΔG_{H^*} value alone is hardly sufficient to describe the apparent HER activity in alkaline solutions. In this case, besides the formation of the H* state, the water dissociation kinetics would also affect the overall reaction rate leading to the experimentally observed activity trend (Figure 6b). At this stage, association of the classical microkinetic model (applying ΔG_{H^*} as an activity descriptor) with the newly considered transition-state theory (applying ΔG_B as an activity descriptor) gives a qualitative confirmation of the sluggish kinetics of hydrogen evolution in alkaline solutions on Pt/C electrocatalysts, and more importantly, explains the underlying mechanism of the better catalytic activity of Ru_{fcc} present in $Ru/C_3N_4/C$ electrocatalysts.

■ CONCLUSION

Using hydrogen evolution as a probe reaction, we correlated the apparent catalytic activity of a cost-effective but highly efficient Ru electrocatalyst with its anomalous crystalline structure and inherent reaction energetics. By identifying the significant influence of water dissociation on the overall HER activity of different metal surfaces, we elucidated the poorly studied HER process in alkaline media through the association of the classical microkinetic model with the transition-state theory. Both experimental data and theoretical computation demonstrate that a special kind of carbon-based material (e.g., $g\text{-}C_3N_4$) can induce an anomalous crystalline structure of a transition metal (e.g., Ru) with having very high catalytic

DOI: 10.1021/jacs.6b11291
J. Am. Chem. Soc. 2016, 138, 16174−16181

activity. Therefore, this study opens a new avenue for the design of a wide variety of solid catalysts for broader heterogeneous and electrocatalytic applications.

■ ASSOCIATED CONTENT

Supporting Information

The Supporting Information is available free of charge on the ACS Publications website at DOI: 10.1021/jacs.6b11291.

More materials characterization, electrochemical measurements, computational results (PDF)

■ AUTHOR INFORMATION

Corresponding Author

*s.qiao@adelaide.edu.au

ORCID

Yan Jiao: 0000-0003-1329-4290

Mietek Jaroniec: 0000-0002-1178-5611

Shi-Zhang Qiao: 0000-0002-4568-8422

Author Contributions

⊥These authors contributed equally.

Notes

The authors declare no competing financial interest.

■ ACKNOWLEDGMENTS

The authors gratefully acknowledge financial support by the Australian Research Council (ARC) through the Discovery Project programs (DP160104866, DP140104062, DP130104459, and DE160101163). NEXAFS measurements were performed on the soft X-ray beamline at Australian Synchrotron. DFT calculations were carried out using the NCI National Facility systems through the National Computational Merit Allocation Scheme.

■ REFERENCES

(1) Nørskov, J. K.; Studt, F.; Abild-Pedersen, F.; Bligaard, T. Catalyst Structure. In *Fundamental Concepts in Heterogeneous Catalysis*; John Wiley & Sons, Inc: Hoboken, NJ, 2014; pp 138−149.

(2) Calle-Vallejo, F.; Loffreda, D.; Koper, M. T. M.; Sautet, P. *Nat. Chem.* **2015**, *7*, 403−410.

(3) Norskov, J. K.; Bligaard, T.; Rossmeisl, J.; Christensen, C. H. *Nat. Chem.* **2009**, *1*, 37−46.

(4) Stamenkovic, V. R.; Fowler, B.; Mun, B. S.; Wang, G.; Ross, P. N.; Lucas, C. A.; Marković, N. M. *Science* **2007**, *315*, 493−497.

(5) Somorjai, G. A.; Materer, N. *Top. Catal.* **1994**, *1*, 215−231.

(6) Liu, J.-X.; Su, H.-Y.; Sun, D.-P.; Zhang, B.-Y.; Li, W.-X. *J. Am. Chem. Soc.* **2013**, *135*, 16284−16287.

(7) Haruta, M.; Yamada, N.; Kobayashi, T.; Iijima, S. *J. Catal.* **1989**, *115*, 301−309.

(8) Medford, A. J.; Wellendorff, J.; Vojvodic, A.; Studt, F.; Abild-Pedersen, F.; Jacobsen, K. W.; Bligaard, T.; Nørskov, J. K. *Science* **2014**, *345*, 197−200.

(9) Behrens, M.; Studt, F.; Kasatkin, I.; Kühl, S.; Hävecker, M.; Abild-Pedersen, F.; Zander, S.; Girgsdies, F.; Kurr, P.; Kniep, B.-L.; Tovar, M.; Fischer, R. W.; Nørskov, J. K.; Schlögl, R. *Science* **2012**, *336*, 893−897.

(10) Jiao, Y.; Zheng, Y.; Jaroniec, M.; Qiao, S. Z. *J. Am. Chem. Soc.* **2014**, *136*, 4394−4403.

(11) Jiao, Y.; Zheng, Y.; Jaroniec, M.; Qiao, S. Z. *Chem. Soc. Rev.* **2015**, *44*, 2060−2086.

(12) Marković, N. M.; Ross, P. N., Jr *Surf. Sci. Rep.* **2002**, *45*, 117−229.

(13) Nørskov, J. K.; Rossmeisl, J.; Logadottir, A.; Lindqvist, L.; Kitchin, J. R.; Bligaard, T.; Jónsson, H. *J. Phys. Chem. B* **2004**, *108*, 17886−17892.

(14) Nørskov, J. K.; Bligaard, T.; Logadottir, A.; Kitchin, J. R.; Chen, J. G.; Pandelov, S.; Stimming, U. *J. Electrochem. Soc.* **2005**, *152*, J23−J26.

(15) Conway, B. E.; Tilak, B. V. *Electrochim. Acta* **2002**, *47*, 3571−3594.

(16) Zheng, Y.; Jiao, Y.; Jaroniec, M.; Qiao, S. Z. *Angew. Chem., Int. Ed.* **2015**, *54*, 52−65.

(17) Cook, T. R.; Dogutan, D. K.; Reece, S. Y.; Surendranath, Y.; Teets, T. S.; Nocera, D. G. *Chem. Rev.* **2010**, *110*, 6474−6502.

(18) Walter, M. G.; Warren, E. L.; McKone, J. R.; Boettcher, S. W.; Mi, Q.; Santori, E. A.; Lewis, N. S. *Chem. Rev.* **2010**, *110*, 6446−6473.

(19) Rheinländer, P. J.; Herranz, J.; Durst, J.; Gasteiger, H. A. *J. Electrochem. Soc.* **2014**, *161*, F1448−F1457.

(20) Lewis, N. S.; Nocera, D. G. *Proc. Natl. Acad. Sci. U. S. A.* **2006**, *103*, 15729−15735.

(21) Durst, J.; Siebel, A.; Simon, C.; Hasche, F.; Herranz, J.; Gasteiger, H. A. *Energy Environ. Sci.* **2014**, *7*, 2255−2260.

(22) Greeley, J.; Jaramillo, T. F.; Bonde, J.; Chorkendorff, I.; Norskov, J. K. *Nat. Mater.* **2006**, *5*, 909−913.

(23) Tsai, C.; Chan, K.; Nørskov, J. K.; Abild-Pedersen, F. *Surf. Sci.* **2015**, *640*, 133−140.

(24) Sheng, W.; Zhuang, Z.; Gao, M.; Zheng, J.; Chen, J. G.; Yan, Y. *Nat. Commun.* **2015**, *6*, 5848.

(25) Markovica, N. M.; Sarraf, S. T.; Gasteiger, H. A.; Ross, P. N. *J. Chem. Soc., Faraday Trans.* **1996**, *92*, 3719−3725.

(26) Birry, L.; Lasia, A. *J. Appl. Electrochem.* **2004**, *34*, 735−749.

(27) McKone, J. R.; Sadtler, B. F.; Werlang, C. A.; Lewis, N. S.; Gray, H. B. *ACS Catal.* **2013**, *3*, 166−169.

(28) Kresse, G.; Furthmüller, J. *Comput. Mater. Sci.* **1996**, *6*, 15−50.

(29) Kresse, G.; Hafner, J. *Phys. Rev. B: Condens. Matter Mater. Phys.* **1993**, *47*, 558−561.

(30) Kresse, G.; Hafner, J. *Phys. Rev. B: Condens. Matter Mater. Phys.* **1994**, *49*, 14251−14269.

(31) Kresse, G.; Furthmüller, J. *Phys. Rev. B: Condens. Matter Mater. Phys.* **1996**, *54*, 11169−11186.

(32) Blöchl, P. E. *Phys. Rev. B: Condens. Matter Mater. Phys.* **1994**, *50*, 17953−17979.

(33) Kresse, G.; Joubert, D. *Phys. Rev. B: Condens. Matter Mater. Phys.* **1999**, *59*, 1758−1775.

(34) Perdew, J. P.; Burke, K.; Ernzerhof, M. *Phys. Rev. Lett.* **1996**, *77*, 3865−3868.

(35) Perdew, J. P.; Burke, K.; Ernzerhof, M. *Phys. Rev. Lett.* **1997**, *78*, 1396−1396.

(36) Grimme, S. *J. Comput. Chem.* **2006**, *27*, 1787−1799.

(37) Duverger, E.; Gharbi, T.; Delabrousse, E.; Picaud, F. *Phys. Chem. Chem. Phys.* **2014**, *16*, 18425−18432.

(38) Zheng, Y.; Jiao, Y.; Zhu, Y. H.; Li, L. H.; Han, Y.; Chen, Y.; Du, A. J.; Jaroniec, M.; Qiao, S. Z. *Nat. Commun.* **2014**, *5*, 3783.

(39) Jiang, D.-E.; Du, M.-H.; Dai, S. *J. Chem. Phys.* **2009**, *130*, 074705.

(40) Radmilovic, V.; Gasteiger, H. A.; Ross, P. N. *J. Catal.* **1995**, *154*, 98−106.

(41) Kitchin, J. R.; Nørskov, J. K.; Barteau, M. A.; Chen, J. G. *J. Chem. Phys.* **2004**, *120*, 10240−10246.

(42) Stradi, D.; Barja, S.; Diaz, C.; Garnica, M.; Borca, B.; Hinarejos, J. J.; Sanchez-Portal, D.; Alcami, M.; Arnau, A.; de Parga, A. L. V.; Miranda, R.; Martin, F. *Phys. Rev. B: Condens. Matter Mater. Phys.* **2013**, *88*, 245401.

(43) Jacobs, K.; Zaziski, D.; Scher, E. C.; Herhold, A. B.; Alivisatos, P. A. *Science* **2001**, *293*, 1803−1806.

(44) Sun, S.; Murray, C. B.; Weller, D.; Folks, L.; Moser, A. *Science* **2000**, *287*, 1989−1992.

(45) Kim, J.; Lee, Y.; Sun, S. *J. Am. Chem. Soc.* **2010**, *132*, 4996−4997.

(46) Kusada, K.; Kobayashi, H.; Yamamoto, T.; Matsumura, S.; Sumi, N.; Sato, K.; Nagaoka, K.; Kubota, Y.; Kitagawa, H. *J. Am. Chem. Soc.* **2013**, *135*, 5493−5496.

(47) Feibelman, P. J. *Science* **2002**, *295*, 99−102.

(48) Chen, G.; Zhang, J.; Gupta, A.; Rosei, F.; Ma, D. *New J. Chem.* **2014**, *38*, 1827−1833.
(49) Thomas, A.; Fischer, A.; Goettmann, F.; Antonietti, M.; Muller, J.-O.; Schlogl, R.; Carlsson, J. M. *J. Mater. Chem.* **2008**, *18*, 4893−4908.
(50) Fan, X.; Zhou, H.; Guo, X. *ACS Nano* **2015**, *9*, 5125−5134.
(51) Feng, L.; Vrubel, H.; Bensimon, M.; Hu, X. *Phys. Chem. Chem. Phys.* **2014**, *16*, 5917−5921.
(52) Ma, L.; Ting, L. R. L.; Molinari, V.; Giordano, C.; Yeo, B. S. *J. Mater. Chem. A* **2015**, *3*, 8361−8368.
(53) Danilovic, N.; Subbaraman, R.; Strmcnik, D.; Chang, K.-C.; Paulikas, A. P.; Stamenkovic, V. R.; Markovic, N. M. *Angew. Chem., Int. Ed.* **2012**, *51*, 12495−12498.
(54) Sheng, W.; Myint, M.; Chen, J. G.; Yan, Y. *Energy Environ. Sci.* **2013**, *6*, 1509−1512.
(55) Colmenares, L.; Jusys, Z.; Behm, R. J. *Langmuir* **2006**, *22*, 10437−10445.
(56) Green, C. L.; Kucernak, A. *J. Phys. Chem. B* **2002**, *106*, 1036−1047.
(57) Laursen, A. B.; Patraju, K. R.; Whitaker, M. J.; Retuerto, M.; Sarkar, T.; Yao, N.; Ramanujachary, K. V.; Greenblatt, M.; Dismukes, G. C. *Energy Environ. Sci.* **2015**, *8*, 1027−1034.
(58) Wolfschmidt, H.; Paschos, O.; Stimming, U. Hydrogen Reactions on Nanostructured Surfaces. In *Fuel Cell Science*; John Wiley & Sons, Inc.: Hoboken, NJ, 2010; pp 1−70.
(59) Hammer, B.; Nørskov, J. K. Theoretical surface science and catalysis—calculations and concepts. In *Advances in Catalysis*; Academic Press: Cambridge, MA, 2000; Vol. *45*, pp 71−129.

DOI: 10.1021/jacs.6b11291
J. Am. Chem. Soc. 2016, 138, 16174−16181